SHARAD-based detection and estimation of water-ice content in Korolev crater at the north pole of Mars

Yongjiu Feng, Yiyan Dong, Rong Wang, Yuze Cao, Peiqi Wu, Shurui Chen, Jingbo Sun, Yuhao Wang, Mengrong Xi, Xiaohua Tong

Abstract—The quest for water-ice is critical in the scientific exploration of Mars, as areas where water reservoirs have been identified could be attractive landing sites for future missions. Korolev crater is located at the Martian north pole, and the interior of the crater is known for its distinct layer of bright deposits exposed at the surface, probably composed of water-ice and rocks. Although studies have estimated the depth of the deposits, the effective volume of ice remains undisclosed. We quantified the volume of water-ice within Korolev crater using SHARAD data, supported by the global MOLA DEM and Context Camera imagery. We applied MOLA data to simulate clutter for 69 SHARAD tracks and improved the identification of radar surface echoes and subsurface reflections. Further, we extracted 18 tracks with discernible surface and subsurface echoes to calculate the dielectric constant for mapping the depth of the ice cover. Spatial visualization was accomplished by superimposing the dielectric constant map onto Korolev crater's 3D topography, unveiling a trend from north to south, with values of the constant dropping from 4.42 to 2.84. The dielectric constant's least-squares solution of 3.565 corresponds to a water-ice content in the range of 50-88.5%, depending on an unknown portion of rock and porosity of the material, confirming earlier inversion results of SHARAD data. Our method presents a viable approach for Martian water-ice detection, and contributes insights into the subsurface water-ice deposits and its dielectric constants. These findings offer critical scientific data to support forthcoming exploration missions (e.g. China's Tianwen-3).

Index Terms—Martian water-ice, orbiter microwaves, dielectric constant, SHARAD, Korolev crater.

I. INTRODUCTION

SCIENTIFIC exploration of deep space has been set off another round of boom in the last decade [1-4], where water-ice exploration is indeed one of the key objectives. The detection of Martian water-ice is paramount for unraveling the planet's geologic history and assessing its potential to harbor life, acting as a key indicator in the search for life on Mars [5, 6]. Water-ice reserves are believed to be plentiful in the mid- and high-latitude regions of Mars, particularly within noteworthy craters like Korolev, Milankovic, and Louth [7-9]. These craters' ice deposits are so extensive that they are observable via optical remote sensing techniques. The mid-latitude zones of Mars experience severe pressure and temperature fluctuations, rendering the water-ice there unstable. Conversely, the poles, with their consistently low temperatures, harbor stable water-ice on the Martian surface [10-12]. Korolev crater, in particular, stands out as the largest and most well-preserved crater near the north pole of Mars, spanning over 80 km in diameter and reserving substantial water-ice [7]. Investigating the water-ice content within Korolev crater is thus essential for enhancing the selection of future Mars landing sites and advancing the search for evidence of life.

Remote sensing stands as a critical technique for detecting Martian water-ice, complementing in situ methods. The technique consists of three main detection modes, namely neutron detection, optical detection and radar detection [13-15]. Neutron detection probes water-ice by using neutron spectroscopy to examine water-equivalent hydrogen in the Martian regolith. For example, Feldman and colleagues [16] investigated Global distributions of neutron fluxes during late southern summer and northern winter using the Mars Odyssey Neutron Spectrometer. However, However, the relatively low spatial resolution of neutron soundings, typically on the order of a few hundred kilometers, and their susceptibility to atmospheric interferences make them deficient in pinpointing water-ice deposits. Optical detection is often used to examine the water-ice distribution because of its relatively high resolution, among them the most widely applied images are Compact Reconnaissance Imaging Spectrometer for Mars (CRISM), High Resolution Imaging Science Experiment (HIRISE), and Context Camera imagery (CTX). For example, Brown and colleagues [17, 18] used CRISM to quantify water-ice deposits in the Martian north polar region during spring and summer. In contrast, radar can detect subsurface water-ice deposits through its superior penetration capability. Typically, scientists have employed SHARAD to examine the thickness of sedimentary layers in Promethei Lingula in the south pole of Mars [19], and to examine the subsurface structures in the Planum Boreum [20]. Evidently, neutron detection has a low resolution and optical detection is unable to examine water-ice

in the subsurface, while radar detection has both better spatial resolution and the ability to probe the water-ice signal underneath, making it a better my choice when faced with the exploration of water-ice in subsurface of the crater on Mars.

Active radar instruments are essential tools aboard Mars orbiters, tasked with discerning the composition and structure of Martian materials through radar echo analysis. These instruments are pivotal for estimating the thickness and density of subsurface stratifications, such as layers of water-ice, rock, and metal [21]. Currently, there are four notable radar payloads in orbit, each with varying detection capabilities: 1) The Radar Imager for Mars' Subsurface Experiment (RIMFAX) on NASA's Mars 2020 Rover can probe approximately 10 meters beneath the surface [22]; 2) The Mars Orbiter Scientific Investigation Radar (MOSIR) aboard China's Tianwen-1 mission has the capacity to detect structures several hundred meters deep [23]; 3) The Shallow Radar (SHARAD) on NASA's Mars Reconnaissance Orbiter (MRO) also reaches several hundred meters below the Martian surface [24]; 4) The Mars Advanced Radar for Subsurface and Ionospheric Sounding (MARSIS) on the European Space Agency's Mars Express can penetrate to depths of about 3.7 km [25, 26]. Among these, SHARAD, operating at 15-25 MHz with a vertical resolution of 15 meters, provides a finer resolution in comparison to MARSIS, which operates at 1.3-5.5 MHz with a vertical resolution of 150 meters, making SHARAD particularly adept at detecting subsurface Martian water-ice [24]. Leveraging the radar remote sensing data from these instruments enables the identification of layered sedimentary structures and water-ice composites within the polar ice caps of Mars.

It was evident that radar data plays a crucial role in detecting Martian regolith structure and deposits. Typically, Picardi and colleagues [27] first applied clutter simulation methods to detect the bottom structure and deposit depth of Planum Boreum through MARSIS. Utilizing MARSIS data, scientists have generated three-dimensional representations of Mars' subsurface structures and compositions [25]. SHARAD data has been instrumental in detecting subsurface water-ice deposits at various latitudes, as well as uncovering the stratified nature of the polar ice sheets, potentially housing water-ice mixtures [28-30]. Further studies have employed SHARAD to quantify the volume and depth of Martian subsurface water-ice [12, 31]. For instance, Stuurman and colleagues [12] combined SHARAD data with morphological analyses to estimate a substantial 14,300 km³ reservoir of water-ice in Utopia Planitia region of Mars. In addition, Brothers and colleagues [31] applied three-dimensional stratigraphic methods to SHARAD data, estimating that Korolev crater contains between 1,400 and 3,500 km³ reservoir of water-ice, with a depth reaching 1.8 km. These investigations primarily focus on the volume and storage depth of water-ice within Martian craters. However, since water-ice is often mixed with rock and air, differentiating these components is essential for a more precise quantification of net water-ice content. The literature indicates that radar signal anomalies in Martian regolith could result from varying mixtures of water-ice, rock, or air-filled pores. Stillman and colleagues [32] suggested employing a three-phase power relationship to leverage constrained radar readings, which can help distinguish among these components. Such a method could lead to more accurate estimations of net water-ice content within Martian water-ice mixtures [33].

Large craters on Mars are significant reservoirs for water-ice, making the precise quantification of their net water-ice content a pressing scientific challenge. In utilizing SHARAD data to infer the dielectric constants and water-ice content of Mars' shallow subsurface, two critical issues must be addressed: 1) Is it possible to accurately assess the dielectric constant of Korolev crater and its associated net water-ice content? 2) What are the features and trends of the spatial distribution of dielectric constants in Korolev crater? To tackle these questions, we embarked on an in-depth study of Korolev crater, located at the north pole of Mars, employing active radar data from SHARAD. Our approach involved the facet approximation method, which segments the terrain to calculate surface echoes for clutter simulation. By comparing radargrams with cluttergrams, we could mitigate clutter caused by the crater walls and pinpoint the true subsurface reflectors. This enabled the extraction of both surface and subsurface echo information and the subsequent calculation of dielectric constants. For the inversion of water-ice content, we applied a three-phase mixed dielectric model. This research endeavors to deliver a meticulous assessment of the dielectric constants and net water-ice content in Korolev crater, enhancing the fidelity of data for guiding future Martian explorations and aiding in the selection of landing sites for forthcoming missions (e.g. China's Tianwen-3).

II. METHODS

To determine the dielectric constants and water-ice content within Martian craters, we must first isolate the clutter introduced by the crater walls. This is achieved through the analysis of radargrams and cluttergrams, allowing for the extraction of pertinent surface and subsurface echoes. Such an analysis facilitates the identification of subsurface reflectors and the computation of dielectric constants. Additionally, we employ a three-phase mixed dielectric model to invert the water-ice content, with the inversion results subsequently validated by. Fig. 1 outlines the methodology for inverting water-ice content in Korolev crater using SHARAD data: a) Input and preprocess SHARAD data, b) Utilize ephemeris data for terrain extraction and segmentation, then calculate radar echo power to generate a cluttergram, and c) Compute the dielectric constant and apply the three-phase mixed dielectric model to invert water-ice content.
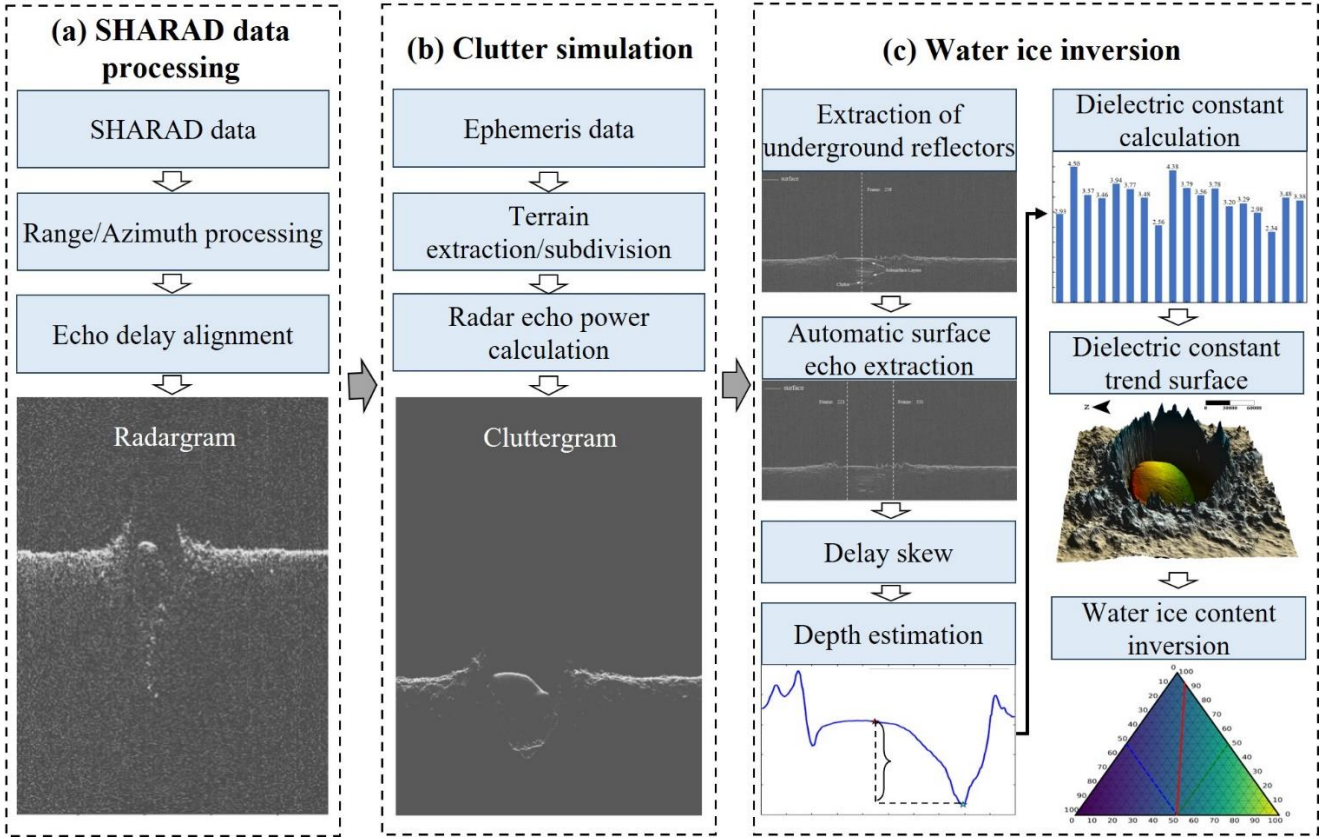
Fig. 1. Technical procedure for inversion of water-ice content in Korolev crater by integrating SHARAD and ephemeris datasets.

A. Terrain clutter simulation methods

Within the radar footprint (the ellipse in Fig. 2a, denoted as P), diverse terrain features generate clutter, which can obscure subsurface echoes and complicate the detection of actual subsurface targets. This necessitates the simulation and identification of clutter. Initially, radar echoes from the planetary surface within a footprint are numerically computed by dissecting the surface terrain within the footprint. A common approach involves fitting the continuous surface terrain with an array of regular, discrete facets [34], known as the facet approximation method, depicted in Fig. 2b. To accurately model the planetary surface, we established a grid of points on the surface (at the bottom of Fig. 2b) with a resolution corresponding to the facet length. As Fig. 2b illustrates, five points on the grid, including one central point (point 1) and four peripheral points (points 2 to 5), are employed to ascertain the facet's orientation. The peripheral points also serve as centers for the adjacent facets. The gray facet is tangential to the actual surface at its central point (point 1), with the slope determined by the elevations of the peripheral points. To describe a specific facet in terms of its center coordinates, the formula can be that given by [35]:

$$d_r = \sqrt{(z_i - h)^2 + [(x_i - x_0)^2 + (y_i - y_0)^2] + (1 + h/R_p)}$$

(1)

$$\theta = \frac{\pi}{2} + tan^{-1}\left[\frac{\sqrt{(x_i - x_0)^2 + (y_i - y_0)^2}}{(z_i - h)}\right]$$

(2)

$$\emptyset = tan^{-1}\left(\frac{x_i - x_0}{y_i - y_0}\right)$$

(3)

where d_r denotes the distance from the radiosonde antenna to the facet, (x_i, y_i, z_i) denotes the coordinates of a point i on the facet, (x_0, y_0) denotes the coordinates of the orbiter, h denotes the height of the orbiter, R_p denotes the radius of the planet, θ denotes the angle of incidence, and $\emptyset$ denotes the azimuth angle.

By modeling the surface terrain, we can determine the position, orientation, and elevation of individual facets. The aggregate surface echo is the cumulative sum of echoes reflected from each facet. In the time domain, the echo simulation for a facet within a specific frame i at a given moment t_i can be formulated as [35]:

$$\begin{cases} E(i,t) = A \sum \rho(\theta, \varepsilon_r) \cos^A \theta \frac{\delta(t_i - 2d_r)}{d_r^4} \\ \rho(\theta, \varepsilon_r) = \left|\frac{\cos\theta - \sqrt{\varepsilon_r - \sin^2\theta}}{\cos\theta + \sqrt{\varepsilon_r - \sin^2\theta}}\right|^2 \end{cases}$$

(4)

where E denotes the power, ρ denotes the relative Fresnel coefficient of the facet, θ denotes the local angle of incidence, ε_r denotes the dielectric constant, d_r can be calculated from (1), and the constant A denotes the amplitude of the emitted signal. Within radar footprint in each frame, the simulated echo for a frame is the sum of all surface echoes that have incidence angles less than 10 degrees. A cluttergram is produced by compiling the simulated echo signal for each

R: The radar on the satellite **R1-R2**: Nadir echo — Specular reflection **1**: Facet center point

P: Footprint **C1-C2**: Non-nadir echo — Clutter **2**: Facet north point

S: Martian Surface **T1**: Across track **3**: Facet south point

T2: Along track **4**: Facet west point

5: Facet east point

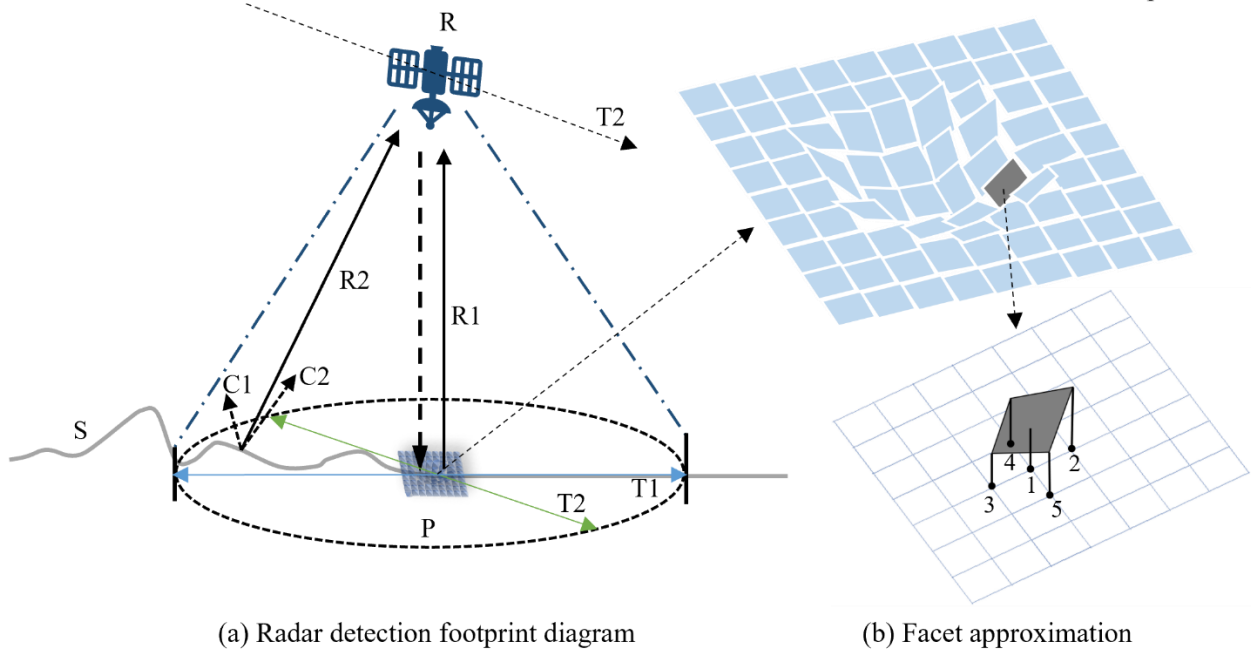(a) Radar detection footprint diagram (b) Facet approximation

Fig. 2. Examples of orbiter radar footprints and the facet approximation method used to compute echoes.

frame, thereby combining them into a single representation.

On flat planetary surfaces, a first return typically originates from the nadir point. However, with even minor surface slopes, a first return may instead come from positions other than the nadir, resulting in clutter. Topographic data can be instrumental in predicting the origins of these first returns from the surface, which is critical when determining the location of the reflector. The fundamental approach involves calculating the distance between the orbiter's coordinates and the center of each facet within the footprint for each frame. This is followed by computing the time-delay based on this distance, aligning the last frame, and identifying the facet center point with the minimum delay time (which is anticipated to be the first echo received) as the position of the first return. This process is described by [36]:

$$\begin{cases} d_i(j) = \sqrt{(x(i) - x_i(j))^2 + (y(i) - y_i(j))^2 + (z(i) - z_i(j))^2} \\ t_{shift(i)} = (max(R_{SC}(i) - R_{EP}(i)) - (R_{SC}(i) - R_{EP}(i))) * \frac{2}{c} \\ sample_{first-return} = min\left(d_i(j) * \frac{2}{c} + t_{shift(i)}\right)/\Delta t \end{cases}$$

$$(5)$$

where $d_i(j)$ denotes the distance of the i-th frame orbiter from the facet j, $(x_i(j), y_i(j), z_i(j))$ denotes the i-th frame orbiter coordinates, $t_{shift(i)}$ denotes the time offset of the i-th frame, R_{SC} and R_{EP} denote the radius of the orbiter from the center of

Mars and the radius of the Martian ellipsoid respectively, c denotes the speed of light, $sample_{first-return}$ denotes the number of samples corresponding to the simulated first return, and Δt denotes the sampling frequency (for SHARAD, Δt is 37.5 ns).

B. Echo information extraction method

Upon acquiring the cluttergram, it is imperative to distinguish between surface and subsurface echoes within the radargram. The number of samples (denoted as *sample*) from the radargram can be translated into a time-delay (*timedelay*) by multiplying with the sampling frequency (*Δt*) encapsulated by [35]:

$$timedelay = sample \times \Delta t \qquad (6)$$

Each frame of the radargram represents a vertical cross-section of the planetary surface. A radar echo is generated when the transmitted wave encounters a sharp discontinuity in the dielectric constant. Predominantly, a first return in a radargram is the surface reflection because clutter, caused by terrain irregularities, and subsurface echoes are delayed due to their increased travel distance from the reflector to the spacecraft. Furthermore, the amplitude of surface echoes typically exceeds that of clutter or subsurface echoes. Consequently, assuming that the first return indicates the surface reflection, we establish a discrimination criterion

(N) to localize the surface echo, as defined by [35]:

$$N(i) = \frac{|S(i)|^2}{mean(|S(i-1:i-winsize)|^2)} \quad (7)$$

where S denotes the radar signal of a particular frame, i denotes the time index within that frame, and $N(i)$ denotes the comparison between the i-th sample and the average of the signal in the *winsize* sampling window that arrived before it. The value of $N(i)$ is largest when $|S(i)|^2$ is largest and $mean(|S(i-1:i-winsize)|^2)$ (representing the noise power level) is smallest. This scenario is typically fulfilled exclusively by surface echoes, rendering any preceding echo as noise. Once the surface signal is pinpointed, the amplitude of the surface echo can be readily extracted.

Nevertheless, subsurface radargram analysis is often complicated by attenuation of the radar waves as they traverse the geological medium, leading to signal gradients and elevated background noise. This complexity can result in inaccurate extraction of subsurface layers based solely on intensity. To mitigate this issue and enhance the accuracy of subsurface layer identification, we employed the open-source software Radar Analysis Graphical Utility (RAGU) (https://doi.org/10.5281/zenodo.4437841) for visual assessment and manual delineation. After identifying the relevant subsurface echoes, we applied the RAGU software to manually select a sequence of sample echo points to generate the reflector, and converted the time-delay by calculating the coordinate difference between the sample surface reflector and the subsurface reflector.

C. Calculation of dielectric constant

The depth to the subsurface reflector is determined by integrating geological context and topographical data, while dielectric constants are derived by analyzing time-delay data from radargrams. The relationship linking time-delay and depth with dielectric constant is articulated as [12]:

$$\frac{c}{\sqrt{\varepsilon_r}} = \frac{2d}{t} \quad (8)$$

where d is the echo depth and t is the two-way travel time.

In estimating the depth of the subsurface reflector, we designated the first return point as the reference for the surface elevation of the deepest subsurface layer. We then selected the ephemeris point with the lowest elevation as the basis for the elevation estimation of this layer. By subtracting the two, we derived the depth of the subsurface reflector. We correlated the calculated depth with the radar reflection time-delay between the surface and subsurface to ascertain the wave velocity and, consequently, the dielectric constant of the material overlaying the study area. The linear dependence described in (8) can be reformulated as [12]:

$$\begin{bmatrix} D_1 \\ D_2 \\ \vdots \\ D_n \end{bmatrix} [m] = \begin{bmatrix} d_1 \\ d_2 \\ \vdots \\ d_n \end{bmatrix} \quad (9)$$

where n denotes the number of orbitals after screening, $D=\frac{ct}{2}$ denotes the product of the speed of light (c) and the one-way travel time ($\frac{t}{2}$) for the n orbitals, d denotes the estimations of the depth of the reflector, and $m = \frac{1}{\sqrt{\varepsilon_r}}$ denotes the transmission coefficient of radar signal in the Martian regolith. Due to the potential for redundant solutions when calculating the dielectric constant using multi-track data from the study area, a linear regression via the weighted maximum likelihood least squares approach was employed to derive the least squares estimation for the dielectric constant, expressed as [12]:

$$\begin{cases} m_{L2} = (D^T D)^{-1} D^T d \\ \varepsilon_{rL2} = (\frac{1}{m_{L2}})^2 \end{cases} \quad (10)$$

where m_{L2} denotes the least squares solution of the model parameter m, and ε_{rL2} denotes the least squares fitted value of the dielectric constant ε_r. The assumption is that the measurement errors for the depth (d) are independent and follow a normal distribution. The true standard deviation of the measurement error being unknown, the confidence interval (I) for the dielectric constant is estimated from the residuals of the model [37]:

$$\begin{cases} r = d - Dm \\ v = n - k \\ I = \frac{\|r\|_2}{\sqrt{v}} \end{cases} \quad (11)$$

where r denotes the vector of residual values, v denotes the number of degrees of freedom, n denotes the number of orbitals after screening, and k denotes the number of model parameters.

D. Water-ice content inversion method

The estimated values of the dielectric constant (ε_r) are compared against the modeled dielectric constants of three-phase mixtures comprised of ice, rock, and air (representing empty pore space) with varying volume fractions. This comparison aims to deduce the water-ice compositional content of the medium. The modeling adheres to a power relationship as delineated by [33]:

$$\varepsilon_{mix}^{1/\gamma} = v_{rock}\varepsilon_{rock}^{1/\gamma} + v_{ice}\varepsilon_{ice}^{1/\gamma} + v_{air}\varepsilon_{air}^{1/\gamma} \quad (12)$$

where ε_{mix} denotes the dielectric constant of the three-phase mixture, ε_{rock} denotes the dielectric constant of rock, ε_{ice} denotes the dielectric constant of ice, and ε_{air} denotes the dielectric constant of air; v_{rock} denotes the volumetric content of rock, v_{ice} denotes the volumetric content of ice, v_{air} denotes the volumetric content of air, and γ is an adjustment parameter. The parameter (γ) serves as an empirical adjustment factor. Following the research outlined by Shabtaie and colleagues [38], we utilized $\gamma=2.7$ for ice-air mixtures. This value is also considered applicable to inclusions within any dielectrically inert matrix, which encompasses the expected range of Martian geological media.

III. STUDY AREA AND DATA

The northern mid- to high-latitude region of Mars presents a complex landscape featuring diverse terrain, as depicted in Fig. 3a. This includes prominent mountains such as Phlegra

(a) DEM of Mars North Pole and typical topographic region

(b) Korolev crater on CTX image

(c) Two typical SHARAD radar tracks (s_01308401 and s_01081601)

(d) SHARAD radargram across Korolev Crater (s_ 01308401)

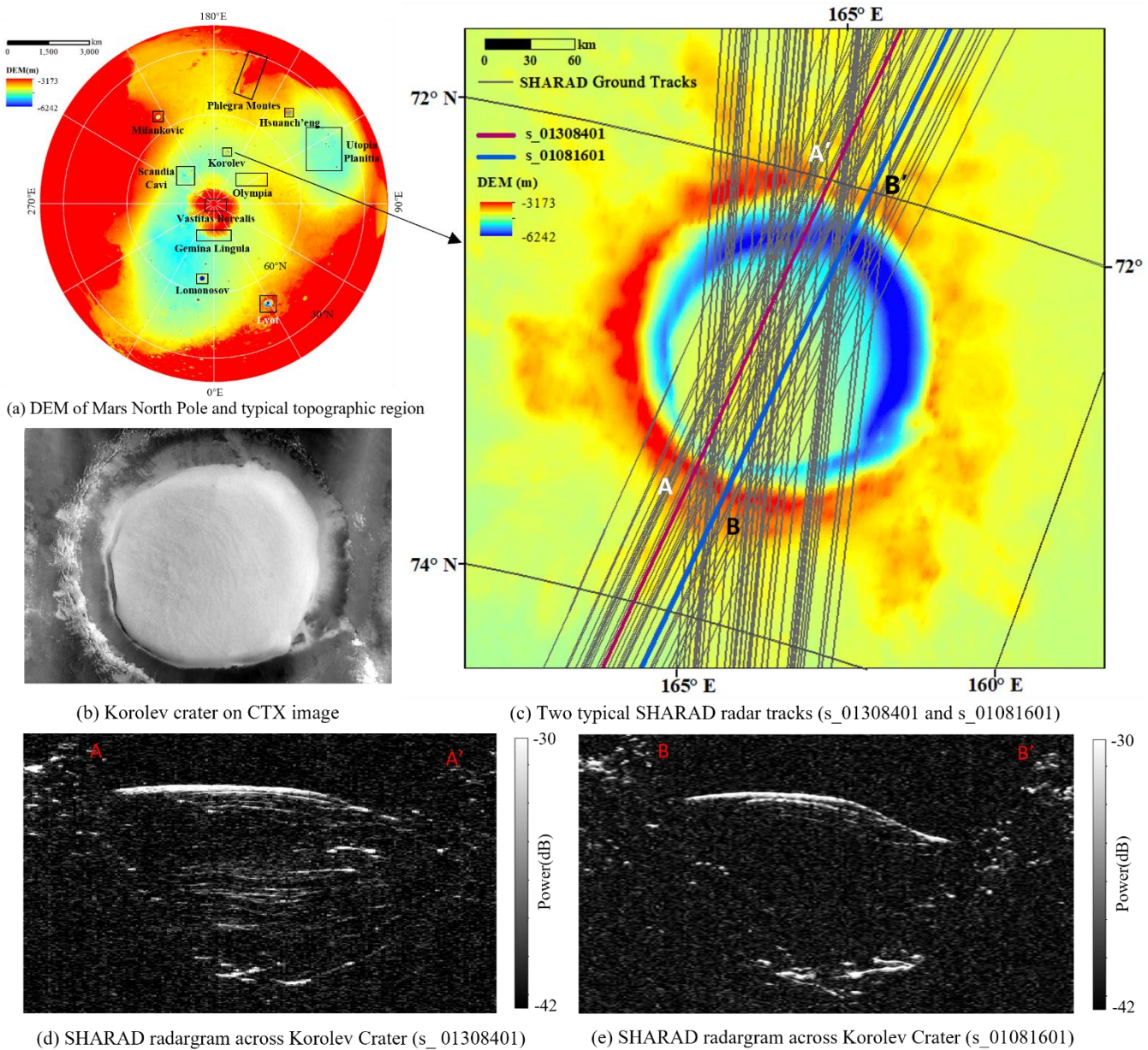(e) SHARAD radargram across Korolev Crater (s_01081601)

Fig. 3. The location of Korolev crater and its associated SHARAD data: (a) typical diverse terrains at the Martian north pole; (b) the CTX image of Korolev crater; (c) the terrain within Korolev crater along with the pertinent 69-track data set, highlighting two representative tracks (in red and blue); (d) a SHARAD radargram that intersects Korolev crater, with points A and A' indicated on track s_01308401; and (e) a SHARAD radargram that intersects Korolev crater, with points B and B' indicated on track s_01081601.

Montes and Gemina Lingula, expansive plains like Olympia Undae and Utopia Planitia, and notable craters, namely Korolev and Lomonosov. Situated at high northern latitudes, Korolev crater, centered at 72.7°N and 164.5°E, is a significant topographical feature with a diameter of approximately 81.4 km. It is believed to contain a substantial deposit of water-ice, ranging from 1,400 to 3,500 km³ and reaching up to 1.8 km in thickness at the crater's center [31]. Radar investigation of the water-ice within Korolev crater is essential to advancing our comprehension of Mars's north polar region. Fig. 3b reveals extensive ice coverage within

Korolev crater as seen in the optical image from CTX. Fig. 3c shows the topography of Korolev crater within the area of study, where we selectively analyzed 69 SHARAD data tracks that satisfied the criteria for data quality and alignment of observation angles against the surface features. Two typical tracks, identified as s_01308401 and s_01081601, are highlighted in this figure. The radar data illustrated in Figs. 3d and 3e offers less straightforward insights when compared to the optical image (Fig. 3b), hence they need to be interpreted together. SHARAD data from orbit s_01308401 and s_01081601 traverses the crater, revealing preliminary

radargrams that portray the reflector as having a distinctly southward-tilted, asymmetric dome shape. Furthermore, Fig. 3e shows the stratigraphic consistency of the horizontal reflector of track s_01081601 appearing uniform from the base to the summit of the crater, exhibiting no marked variations in response to echo time.

Topographic data are essential for clutter simulations, estimation of the first return position, and depth analysis. For these purposes, we employed the DEM MEGDR obtained from the MOLA with a resolution of 128 pixels per degree to serve as the reference DEM. This data was acquired from the TES on board the Mars Global Surveyor orbiter, boasting a resolution of 0.12°. The datasets from SHARAD, MOLA, and CTX are publicly accessible via NASA's PDS, which can be found at https://pds.nasa.gov.

IV. RESULTS

A. Terrain-induced clutter analysis

We conducted clutter simulations on the 69-track dataset using the MOLA DEM and established clutter simulation methodologies to differentiate the genuine subsurface echoes from clutter. The radargrams for two distinct SHARAD data tracks, s_01081601 and s_01308401, are depicted in Figs. 4a and 4c, respectively. Their equivalent MOLA DEM-based clutter simulations are displayed in Figs. 4b and 4d. The first SHARAD data track is associated with the crater segment shown in Fig. 4e, while the second relates to the segment in Fig. 4f. The comparison of radargrams and clutter simulations demonstrates negligible differences in reflected signals between Figs. 4a and 4b, suggesting an absence of notable stratigraphic disparities beneath track s_01081601. In contrast, the comparison of Figs. 4c and 4d indicates a clear distinction between the actual SHARAD echoes and the simulated ones, revealing pronounced and discrete subsurface reflections, which were from below the nadir points. Figs. 4e and 4f provide the simulated positions of the first returns for the two tracks, where most echo points are concentrated near the track lines. This indicates that the majority of the echoes originate near the nadir points along the tracks. Due to the significant elevation disparity between the crater's rim and its interior, some first return points emanate from the crater's wall and are situated at a distance from the track line, correlating with the clutter. We discarded tracks lacking conspicuous subsurface echoes in the radargrams, and selected 18 tracks of SHARAD data exhibiting subsurface echoes for shallow subsurface water-ice detection.
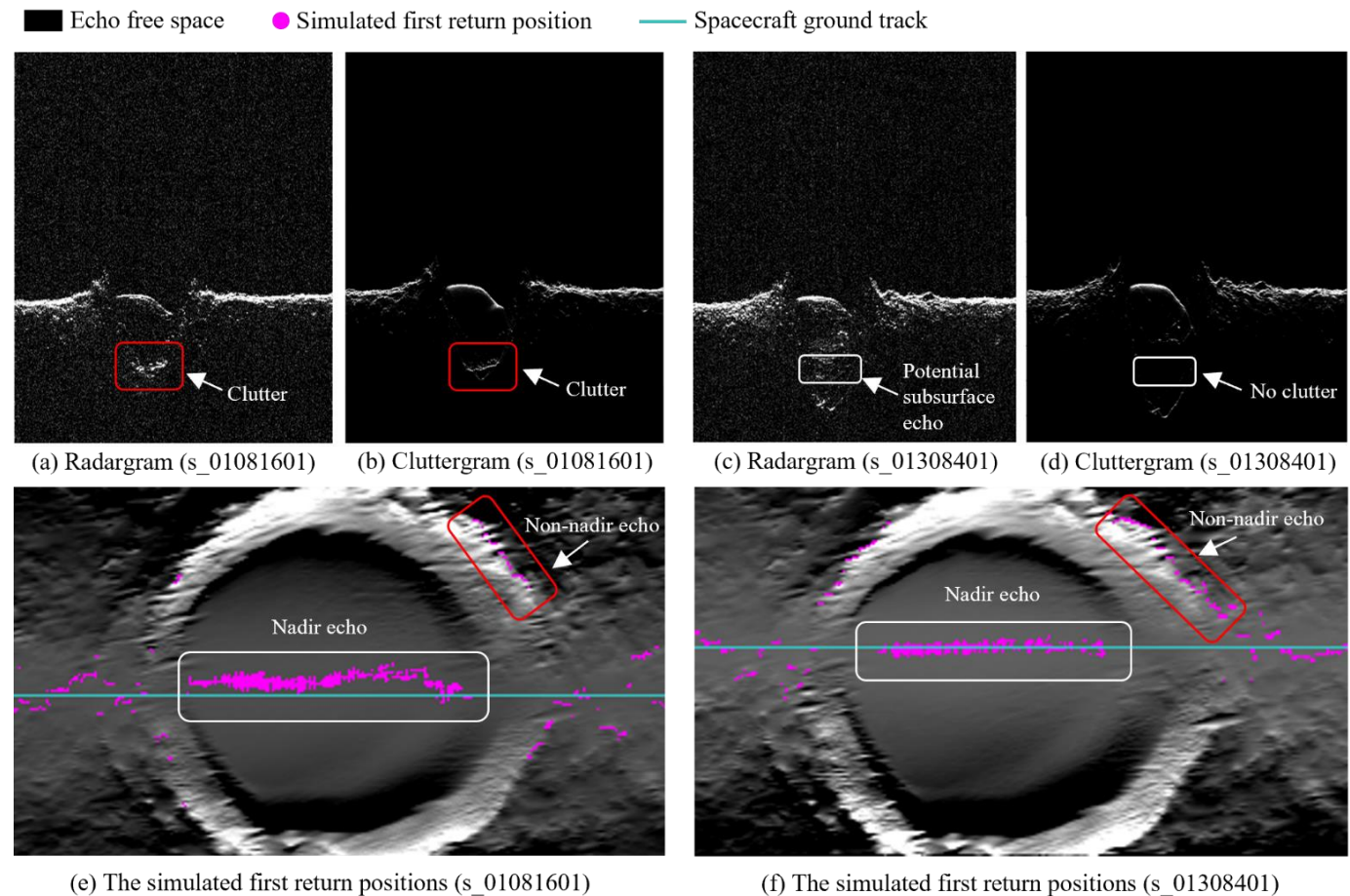

(a) Radargram (s_01081601) (b) Cluttergram (s_01081601) (c) Radargram (s_01308401) (d) Cluttergram (s_01308401)

(e) The simulated first return positions (s_01081601) (f) The simulated first return positions (s_01308401)

Fig. 4. Graphical representation of the radargrams and cluttergrams, compared with their simulated first return positions.

(a) SHARAD radargram and surface-to-subsurface echo extraction results

(b) Waveform and extracted surface echo for frame 221

(c) Waveform and extracted surface-to-subsurface echo for frame 258
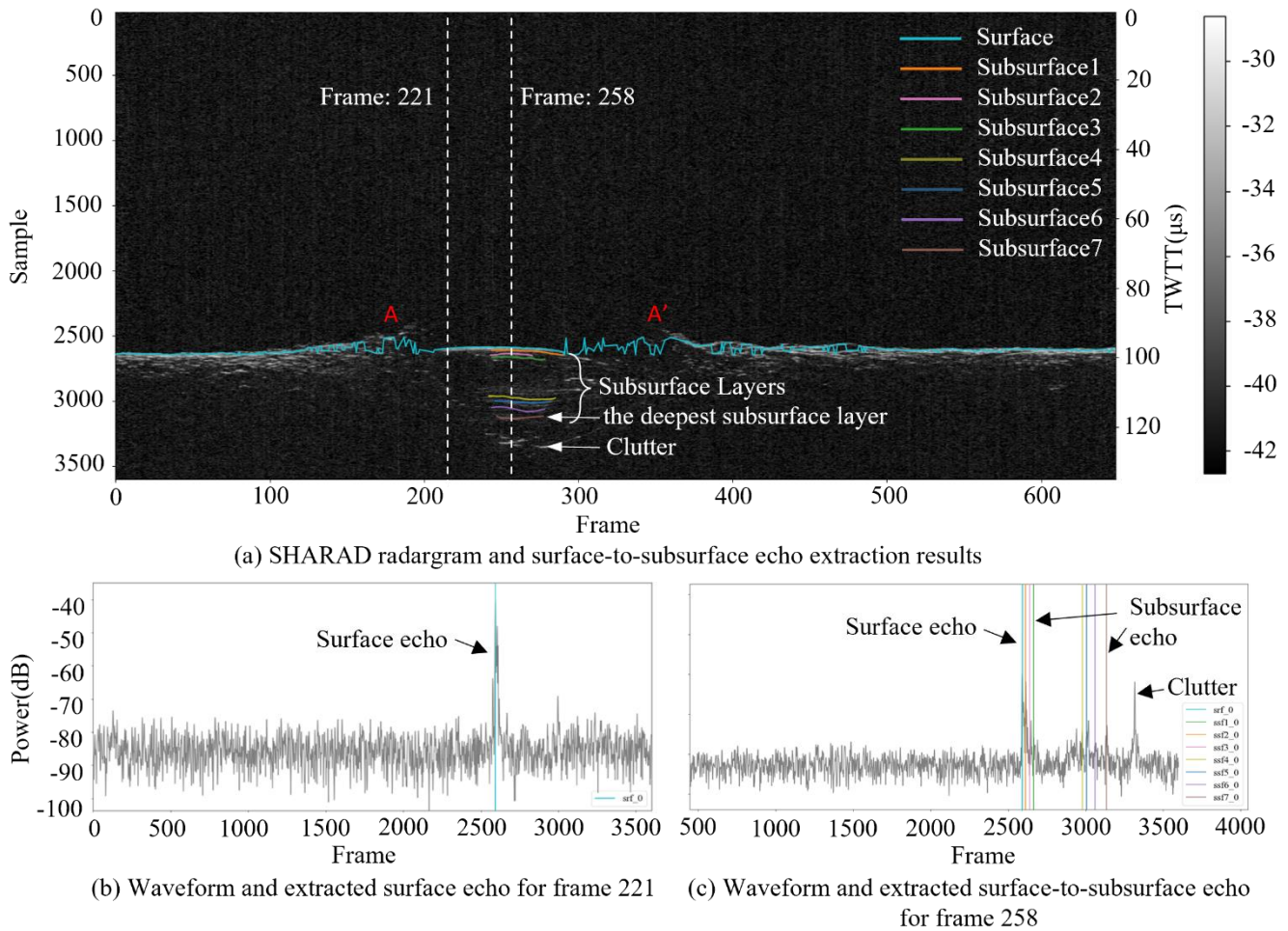
Fig. 5. The extraction of echoes from the surface to subsurface and the corresponding waveforms from radargrams.

B. Echo information extraction

We successfully extracted surface echoes from the 18-track dataset of SHARAD data using (7). Fig. 5 specifically illustrates the surface echo results for track s_01308401 and its characteristics in detail. In Figs. 5a and 5c, the echoes within the frame intervals of approximately 150-200 and 300-400 (corresponding to the crater walls) are characterized by non-smooth curves, suggesting time-delays in the echo transmission. Nonetheless, the water-ice or water-ice mixtures are predominantly found within the central mound of Korolev crater, where signal delays and errors caused by the crater walls have a negligible impact on the accuracy of echo extraction. The blue line in Fig. 5a represents the identified surface echoes, which align with the topographical features of the area. Notably, frame 221 exhibits only surface echoes, while frame 258 contains both surface and subsurface echoes. Consequently, we utilized the data from frame 258 to determine the time-delay difference. Fig. 5b displays the waveform of frame 221 from the radargram, where the blue line marks the position of the detected surface echo at the wave's peak, which possesses the highest power. This peak corresponds to a sample value of 2594 and a time-delay of 97.275 μs.

Fig. 5c presents the waveform for frame 258, where the blue line denotes the extracted surface echo and the other traces represent the extracted subsurface layers. Upon comparison with the clutter simulation in Fig. 4d, it was determined that the subsurface layer at Sample 3355 (shown in Fig. 5c) is attributable to clutter generated by the surface topography, therefore, this layer was excluded from further analysis. This exclusion led to the identification of the deepest subsurface layer, labeled as Subsurface7 in Fig. 5a. The echoes of the surface and subsurface layers in Fig. 5c coincide with the peaks of the power wave, from which we derived a delay of 97.07 μs for the surface layer (denoted as Surface) and 116.62 μs for the deepest subsurface layer (denoted as Subsurface7) in frame 258 of Fig. 5a. This results in a delay difference of 19.55 μs. Fig. 6a displays the screened SHARAD data (exemplified by s_01308401), which illustrated by the red line, exhibiting notable subsurface echoes. The red dots mark the positions of the simulated first return, utilizing track s_01308401 (highlighted by the red line) as a representative case. In this figure, the red pentagram labeled S pinpoints the position of the surface echo (referenced as Surface in Fig. 5a)

(a) s_01308401 on Korolev MOLA DEM
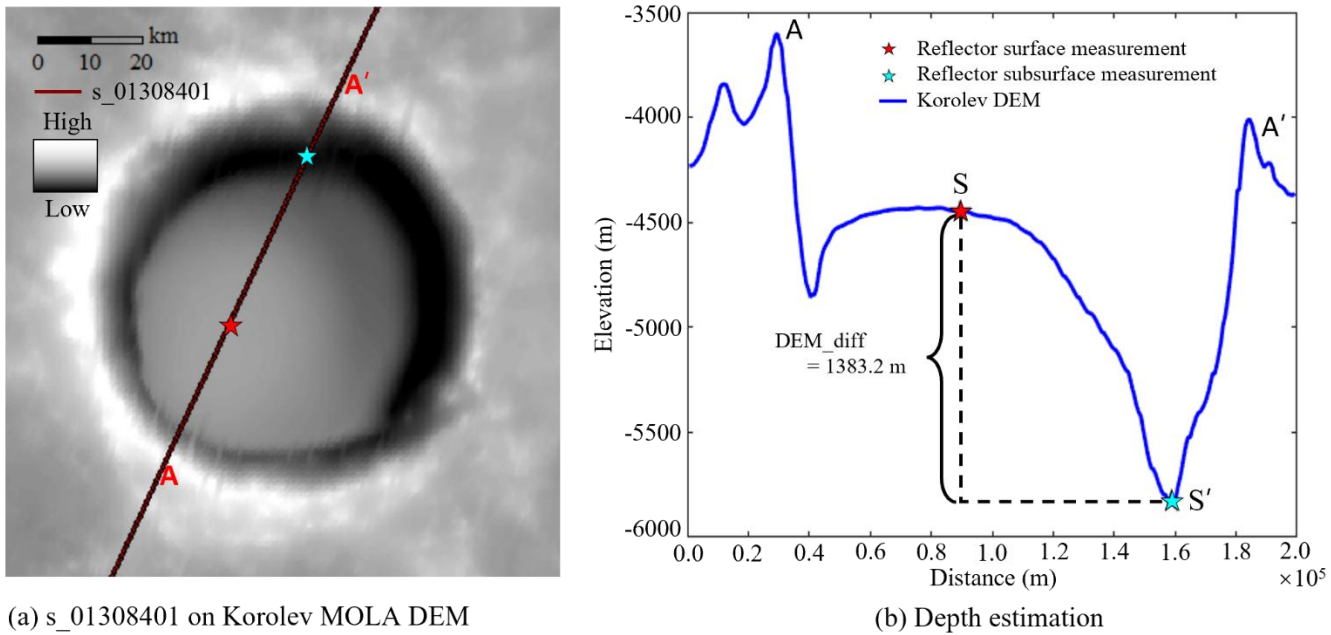

(b) Depth estimation

Fig. 6. One typical SHARAD data (s_01308401) on MOLA DEM and the depth estimation based on data from track s_01308401.

from frame 258 of s_01308401 within Korolev crater, and the blue pentagram labeled S' marks the position of the deepest detected subsurface layer (Subsurface7 in Fig. 5a). This layer's depth, estimated by the DEM profile corresponding to the track (Fig. 6b), is approximately 1383.2 m.

C. Inversion of dielectric constant and water-ice content

Table 1 presents the dielectric constants calculated for each

track using (8). Among these, the depth of the subsurface layer in Korolev crater is estimated to range between 1350 and 1600 m, with a corresponding time-delay difference of about 16 to 20 μs. The calculated dielectric constants span from 2.34 to 4.5, with a majority clustering between 2.93 and 3.94. Uncertainty analysis was conducted on these 18 dielectric

TABLE I

MODEL PARAMETERS AND DIELECTRIC CONSTANTS FOR THE 18 SHARAD TRACKS IN KOROLEV CRATER

| Track No.	Surface elevation (m)	Subsurface elevation (m)	Depth of the reflector (m)	Surface time-delay (μs)	Subsurface time-delay (μs)	Time-delay difference (μs)	Dielectric constant
s_00544201	-4474	-5822	1348	97.30	112.69	15.39	2.93
s_01308401	-4439	-5822	1383	97.07	116.62	19.55	4.50
s_01733001	-4492	-5910	1418	97.51	115.36	17.85	3.57
s_01846401	-4442	-5813	1321	97.38	113.77	16.39	3.46
s_02151001	-4442	-5799	1348	97.26	115.10	17.84	3.94
s_02158201	-4435	-6021	1586	96.95	117.47	20.52	3.77
s_02186601	-4479	-5916	1437	97.36	115.24	17.88	3.48
s_02264401	-4455	-5945	1490	97.25	113.13	15.88	2.56
s_02321102	-4485	-5869	1384	97.25	116.57	19.32	4.38
s_02342201	-4432	-5809	1377	97.21	115.08	17.87	3.79
s_02349401	-4490	-5971	1481	97.46	116.08	18.62	3.56
s_02398901	-4440	-5848	1408	97.19	115.43	18.24	3.78
s_02406102	-4473	-5992	1519	97.45	115.57	18.12	3.20
s_02441102	-4441	-5932	1491	97.14	115.17	18.03	3.29
s_02611201	-4483	-5890	1407	97.80	114.00	16.2	2.98
s_02731201	-4446	-5789	1343	97.42	111.11	13.69	2.34
s_03987901	-4442	-5810	1368	97.05	114.06	17.01	3.48
s_04023501	-4486	-5833	1347	97.48	113.99	16.51	3.38
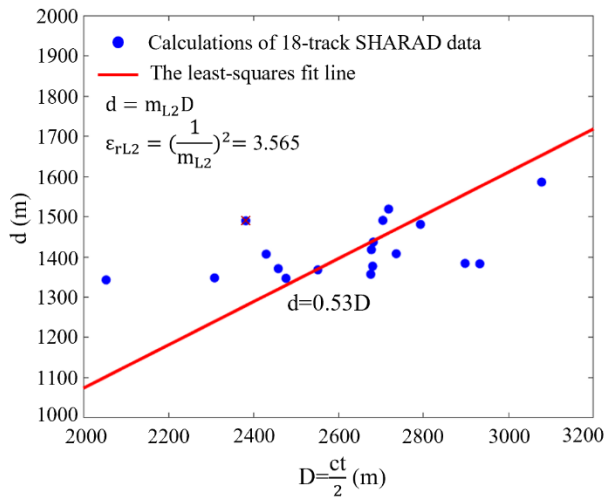
Fig. 7. The least-squares fitting relationship of time-delay (t) and depth (d) for the 18 SHARAD tracks (R^2=0.91).

fit of depth (d) to D $(\frac{ct}{2})$ as described in (9). The least-squares solution yielded a dielectric constant of 3.565 with a 95% confidence interval ranging from 2.813 to 4.317 and an R^2 of 0.91 for the fit, after applying minimal weights to the coarser differences. Fig. 8 illustrates the spatial trend of dielectric constants against the 3D topographic backdrop of the crater. Notably, the crater walls cast darker shadows due to the significant elevation difference between them and the ice dome within. The dielectric constant demonstrates a decreasing trend from north to south within the crater, with the highest values adjacent to the northern crater wall. According to the three-phase mixed dielectric model, regions with lower dielectric constants are likely indicative of higher water-ice content, suggesting that the southern part of the crater may contain a larger volume fraction of water-ice.

It was noted that Mars' shallow surface material comprised a mixture of air, regolith, rock, and water-ice,
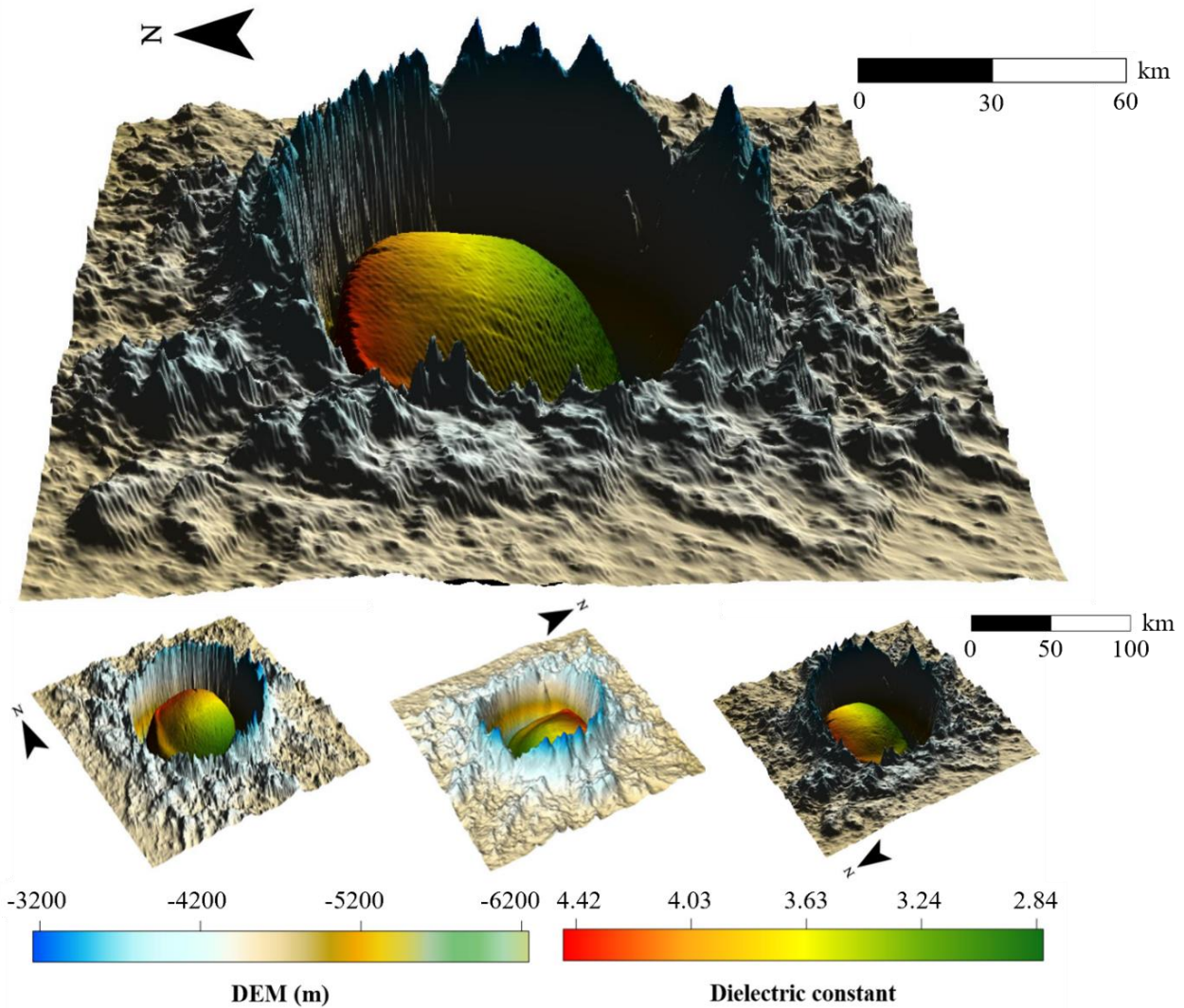
constants following (10), and Fig. 7 shows the least-squares

Fig. 8. The 3D visualization of the dielectric constants in Korolev crater, overlaid on a DEM under different light conditions at multiple angles.

with porosity primarily indicating the presence of air. Modeling work focused on the Phoenix landing site, along with observations from the Viking landing sites of loosely deposited windblown material, hinted at surface porosities around 50%. However, such wind-transported materials may not accurately reflect the porosity of bedrock, and it is understood that subsurface layers exhibit lower porosity than surface deposits. In contrast, recent gravity surveys have reported significantly lower porosities in the near-surface lunar regolith, estimated between 10-20% [39, 40]. Consequently, we have selected the 50% porosity measurement from the Viking site as a conservative upper boundary for porosities within Martian water-ice sediments, in alignment with other Mars-based research [12, 33]. Fig. 9 delineates different regimes of porosity. The bottom-left area of the figure corresponds to geological materials with porosities exceeding 50%, which are relatively uncommon. The bottom-right sector illustrates the range of porous regolith with variable ice content filling the pores. The depicted lines of constant rock content trace a continuum from entirely vacant pore spaces at the bottom of the graph (along the line indicating 0% ice) to fully ice-saturated pores (at the intersection of the rock-content line and the 0% air mark) [33].

The solid red line in Fig. 9 demarcates the inferred compositional makeup of air, water-ice, and rock based on the least squares solution for a dielectric constant of 3.565. The intersections of this solid red line with the axes represent the boundary conditions for water-ice content. Drawing from existing studies on Martian regolith and water-ice [12], the maximal porosity of Mars' shallow subsurface within a three-phase mixed dielectric model is assumed to be 50%. Consequently, the minimal water-ice content is set at 50%, with accompanying air and rock proportions of 22% and 28%, respectively, denoted as C_1 (22, 50, 28). Eliminating air from (12) results in C_2 (0, 88.5, 11.5), which reflects a maximum water-ice concentration of 88.5% and a rock presence of 11.5%, indicating a predominantly high purity of water-ice with a minor rock component. Utilizing the literature and the three-phase mixed dielectric model [33], we estimated the water-ice content within Korolev crater's sediments to fall between 50% and 88.5%.
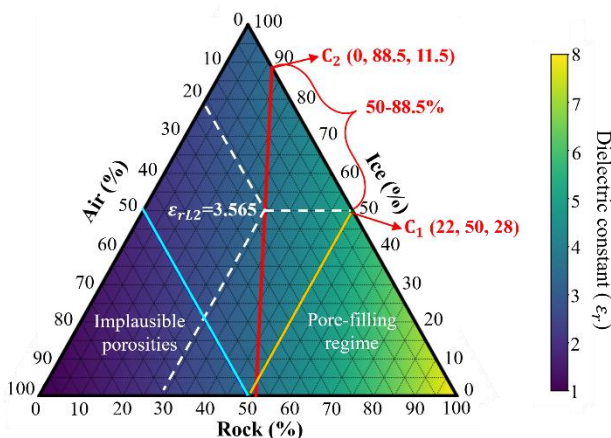

Fig. 9. Projection of water-ice content in Korolev crater utilizing a three-phase mixed dielectric model.

V. DISCUSSION

The mid- and high-latitude regions of Mars are believed to be repositories of water-ice, making Korolev crater, an exceptionally well-preserved crater proximal to the planet's north pole, a significant target for forthcoming Martian scientific investigations. This study delves into the shallow surface layer's physical attributes within Korolev crater utilizing data from the MRO's SHARAD. We employed the facet approximation method to analyze the terrain and calculate surface echoes, thereby facilitating clutter simulation. This enabled us to discern the genuine subsurface layers through a synthesis of radargrams and clutter simulation. Subsequent steps involved the extraction of surface and subsurface echoes and the computation of the dielectric constant. Finally, we conducted an inversion of water-ice content using a three-phase mixed dielectric model.

A. Calculation of dielectric constant

Theoretically, the calculation of the dielectric constant relies on depth and time-delay, while depth calculation can be performed by two methods: 1) depth estimation based on the conversion of the known dielectric constant and time-delay, and 2) depth estimation based on the morphology fitting of the crater. The second method is from Conway and colleagues [41], who calculated the depth of the crater by fitting a bowl-like shape to the bottom of the crater. We defined the depth from the highest point on the surface to the lowest point on the surface as depth 1, and defined the depth from the highest point on the surface to the bottom of the fitted crater as depth 2. In case the dielectric constant is unknown, we solved for its theoretical depth as a benchmark by assuming it to be 3.15 based on the literature [31]. As an example, the s_02264401 data track has a reference depth of 1504.18 m based on the time-delay conversion (Fig. 10a). For the s_02264401 data track, depth 1 is 1489.79 m and depth 2 is 1783.41 (Fig. 10b), so it is clear that depth 1 is much closer to the benchmark (1504.18 m). We therefore adopted depth 1 as the parameter for the calculation of the dielectric constant.

Using the above method, we calculated the crater depth using six tracks (Table 2), and the results show that about 1.8 km of water-ice were deposited inside the crater, which is in agreement with the results of the literature [31, 41]. For example, for the s_02264401 data track, the dielectric constant calculated by depth 1 is 2.56 and that by depth 2 is 1.78, while the former is closer to the 3.15 indicated by the existing literature [31].

### B. Trend of dielectric constant in Korolev crater

We examined the spatial trend of the dielectric constant in Korolev crater based on the measurement points and applied the software Surfer to visualize the dielectric constant from multiple angles in 3D. Fig. 8 shows a very large height difference between the walls of Korolev crater and the ice dome inside the crater, and a decreasing trend in the dielectric constants inside the crater from north to south, with values of the constant dropping from 4.42 to 2.84. Since the dielectric constant in the southern part of the crater is closer to that of
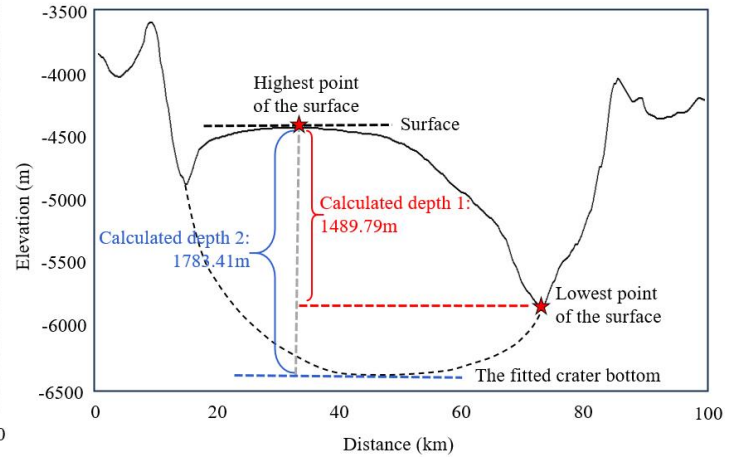
water-ice (3.15), it suggests that the southern part of the crater has a
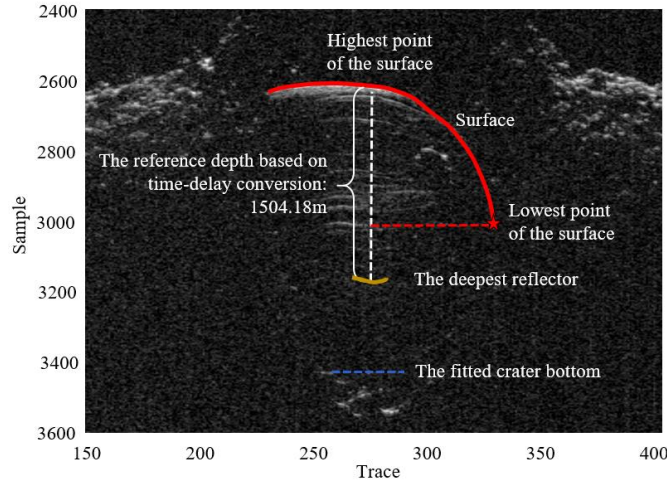
(a) The reference depth based on time-delay conversion using SHARAD of the s_02264401 track

(b) The depth 1 based on the lowest point of the surface and the depth 2 based on the fitted crater related to the s_02264401 track

Fig.10. Comparison of the depths calculated by the two difference methods against theoretical results of time-delay conversion, using the s_02264401 data track as an example.

higher water-ice content than the northern part. Our study confirms the findings of Conway and colleagues [41], who measured the water-ice in Korolev crater using OMEGA spectroscopic data, and also show that the southern part of the crater has a higher water-ice content than the northern part. Since water-ice is continuously deposited to the bottom of the crater, the deepest part of the southern part of the crater may have stored more water-ice, which corroborates the results in Fig. 8.

TABLE II
COMPARISON OF TWO DEPTH CALCULATIONS AND THEIR ASSOCIATED DIELECTRIC CONSTANTS.

Track No.	Depth 1 (m)	Dielectric constant 1	Depth 2 (m)	Dielectric constant 2
s_00554201	1348.00	4.82	1719.64	1.80
s_01308401	1382.96	4.50	1938.13	2.29
s_01733001	1418.02	3.57	1826.27	2.15
s_01846401	1371.99	3.46	1833.19	1.80
s_02151001	1585.84	3.94	1753.64	2.33
s_02264401	1489.79	2.56	1783.41	1.78

C. Selection of dielectric constant values

The dielectric constant, a metric for assessing the speed at which an electromagnetic wave propagates through a medium relative to the velocity in a vacuum, is contingent on the medium's properties. Accurately determining the dielectric constant effectively imposes constraints on the compositional makeup of the radar reflector. Prior research has shown that pure water-ice exhibits a dielectric constant of approximately 3.15 [42], while the dielectric constant for a vacuum, which is analogous to the Martian atmosphere, is 1. Pure basalt, assuming no pore, possesses a dielectric constant of 7.54 [43], and denser basalt variants have recorded dielectric constants nearing 9 [44]. In our study, we ascribed a dielectric constant of 8 to the rock component based on recent findings [45].

Utilizing a three-phase power relationship [32], we estimated the compositional range of water-ice within the medium and depicted our findings on a ternary map illustrating the proportions of air, ice, and rock (Fig. 9).

D. Analysis of water-ice inversion errors

In our analysis of 18 SHARAD tracks over Korolev crater, we computed the dielectric constant based on the depth of the reflector, inferred from time-delay. A least-squares fitting yielded a dielectric constant of 3.565 with a robust correlation coefficient (R^2) of 0.91. However, various sources of error could influence this result.

The three-dimensional modeling of Martian craters by Brothers and colleagues [31] revealed that subsurface layers typically exhibit a domed shape, whereas the deepest layers tend to be nearly flat, averaging a slight slope of only 0.5°. In Korolev crater, its southernmost nadir is perceived as the boundary between the mound materials of the crater and the crater floor, corresponding to the deepest SHARAD reflector. For estimating the depth of this layer, we compared the first return point, representing the surface elevation of the deepest layer, with the lowest ephemeris point, indicative of the estimated lowest elevation, and calculated the difference to determine the subsurface depth. The primary source of error in our depth estimates is the assumption of a perfectly flat crater bottom, which may lead to underestimation. Additionally, inaccuracies in time-delay extraction, due to challenges in identifying the true deepest reflector, could result in minimal differences in calculated time-delays. Consequently, our fitting results are primarily susceptible to errors in depth estimation and time-delay extraction, compounded by difficulties in accurately detecting deeper reflectors on radargrams due to their diminished signal strength.

We estimated the water-ice content within Korolev crater to be between 50% to 88.5% based on the three-phase mixed dielectric model and the dielectric constant's least-squares solution of 3.565. Nevertheless, since our calculation reflects

the overall dielectric constant across the entire detected subsurface interface, from the surface to the subsurface, it may inadvertently incorporate the influence of a dry, weathered layer at the surface. Therefore, our conclusions can only offer a broad characterization of the overall composition, overlooking the nuanced stratigraphy present in the uppermost layers of the subsurface as noted by Bramson and colleagues [33]. These intricacies warrant further detailed investigation in future research endeavors.

VI. CONCLUSIONS

We conducted an investigation into the physical properties of Mars' shallow surface layer, utilizing active radar data from orbiting spacecraft to examine the water-ice content within typical craters. Korolev crater, displaying highly visible icy deposits on its crater floor, is a unique landmark in the north polar region of Mars. In this paper, we have derived new maps of depths and dielectric constants of these icy layers through SHARAD data. Employing the facet approximation method, we deconstructed the terrain to compute surface echoes for clutter simulation. By analyzing the radargrams and cluttergrams, we identified clutter generated by the crater walls, pinpointed the actual subsurface reflectors, and extracted pertinent surface and subsurface echoes. Subsequently, we determined the dielectric constant using a least squares approach, yielding a value of 3.565. Through the application of a three-phase mixed dielectric model for water-ice inversion, we estimated the water-ice content within Korolev crater's sediments to range from 50% to 88.5%. These findings underscore SHARAD's proficiency in detecting water-ice content in Mars' shallow subsurface, down to several hundred meters, surpassing the depth and detection capabilities of multispectral remote sensing techniques.

The contribution of this study are 1) the comparison of two different depth estimation methods and the characterization of the spatial distribution of the dielectric constant inside Korolev crater were found, and 2) the first estimation of the net water-ice content of Korolev, a large Martian crater (50-88.5%) using dielectric constants and three-phase dielectric modeling. The assessment of the water-ice content within Mars' Korolev crater bolsters the evidence of aqueous resources in the planet's shallow subsurface. The dielectric constants and water-ice quantifications gleaned from our research significantly enhance our understanding of Martian hydrology, particularly in estimating the cryospheric composition of large craters in the north polar region. These findings yield critical scientific insights that will aid forthcoming Mars exploration missions and are pivotal for unraveling the planet's climatology, geological evolution, and prospective habitability. Our future endeavors will concentrate on refining water-ice detection techniques to improve precision. We aim to extend our investigations to encompass the entirety of Martian polar regions, both north and south, to achieve a comprehensive mapping of subsurface water-ice distribution.

REFERENCES

[1] S. C. Liu *et al.*, "A Novel Adaptive Spectral Drift Correction Method for Recalibrating the MarSCoDe LIBS Data in China's Tianwen-1 Mars Mission," *IEEE J. Sel. Top. Appl. Earth Observ. Remote Sens.,* Article vol. 16, pp. 5430-5440, 2023.

[2] Y. Q. Wang, H. Xie, C. Wang, X. H. Tong, S. C. Liu, and X. Xu, "Determination of the Spatial Extent of the Engine Exhaust-Disturbed Region of the Chang'E-4 Landing Site Using LROC NAC Images," *IEEE J. Sel. Top. Appl. Earth Observ. Remote Sens.,* Article vol. 16, pp. 468-481, 2023.

[3] H. Chen *et al.*, "CNN-Based Large Area Pixel-Resolution Topography Retrieval From Single-View LROC NAC Images Constrained With SLDEM," *IEEE J. Sel. Top. Appl. Earth Observ. Remote Sens.,* Article vol. 15, pp. 9398-9416, 2022.

[4] Y. Feng *et al.*, "Optimized Landing Site Selection at the Lunar South Pole: A Convolutional Neural Network Approach," *IEEE J. Sel. Top. Appl. Earth Observ. Remote Sens.,* pp. 1-18, 2024.

[5] J. Lasue *et al.*, "Quantitative Assessments of the Martian Hydrosphere," *Space Science Reviews,* Review vol. 174, no. 1-4, pp. 155-212, Jan 2013.

[6] M. Nazari-Sharabian, M. Aghababaei, M. Karakouzian, and M. Karami, "Water on Mars-A Literature Review," *Galaxies,* Review vol. 8, no. 2, p. 45, Jun 2020.

[7] J. C. Armstrong, T. N. Titus, and H. H. Kieffer, "Evidence for subsurface water ice in Korolev crater, Mars," *Icarus,* Article; Proceedings Paper vol. 174, no. 2, pp. 360-372, Apr 2005.

[8] C. M. Dundas *et al.*, "Widespread Exposures of Extensive Clean Shallow Ice in the Midlatitudes of Mars," *J. Geophys. Res.-Planets,* Article vol. 126, no. 3, p. 28, Mar 2021.

[9] A. J. Brown, S. Byrne, L. L. Tornabene, and T. Roush, "Louth crater: Evolution of a layered water ice mound," *Icarus,* Article; Proceedings Paper vol. 196, no. 2, pp. 433-445, Aug 2008.

[10] J. P. Bibring *et al.*, "Perennial water ice identified in the south polar cap of Mars," *Nature,* Article vol. 428, no. 6983, pp. 627-630, Apr 2004.

[11] M. H. Carr, "WATER ON MARS," *Nature,* Review vol. 326, no. 6108, pp. 30-35, Mar 1987.

[12] C. M. Stuurman *et al.*, "SHARAD detection and characterization of subsurface water ice deposits in Utopia Planitia, Mars," *Geophysical Research Letters,* vol. 43, no. 18, pp. 9484-9491, 2016.

[13] T. N. Titus, H. H. Kieffer, and P. R. Christensen, "Exposed water ice discovered near the south pole of Mars," *Science,* Article vol. 299, no. 5609, pp. 1048-1051, Feb 2003.

[14] W. C. Feldman *et al.*, "Global distribution of near-surface hydrogen on Mars," *J. Geophys. Res.-Planets,* Article vol. 109, no. E9, p. 13, Sep 2004.

[15] B. Zhou *et al.*, "The Mars rover subsurface penetrating radar onboard China's Mars 2020 mission," *Earth Planet. Phys.,* Article vol. 4, no. 4, pp. 345-354, 2020.

[16] W. C. Feldman *et al.*, "Global distribution of neutrons from Mars: Results from Mars Odyssey," *Science,* Article vol. 297, no. 5578, pp. 75-78, Jul 2002.

[17] A. J. Brown, W. M. Calvin, P. Becerra, and S. Byrne, "Martian north polar cap summer water cycle," *Icarus,* Article vol. 277, pp. 401-415, Oct 2016.

[18] A. J. Brown, W. M. Calvin, and S. L. Murchie, "Compact Reconnaissance Imaging Spectrometer for Mars (CRISM) north polar springtime recession mapping: First 3 Mars years of observations," *J. Geophys. Res.-Planets,* Article vol. 117, p. 19, Dec 2012.

[19] R. Seu *et al.*, "Accumulation and erosion of Mars' south polar layered deposits," *Science,* Article vol. 317, no. 5845, pp. 1715-1718, Sep 2007.

[20] R. J. Phillips *et al.*, "Mars north polar deposits: Stratigraphy, age, and geodynamical response," *Science,* Article vol. 320, no. 5880, pp. 1182-1185, May 2008.

[21] T. R. Watters *et al.*, "Radar sounder evidence of thick, porous sediments in Meridiani Planum and implications for ice-filled deposits on Mars," *Geophysical Research Letters,* vol. 44, no. 18, pp. 9208-9215, 2017/09/28 2017.

[22] S.-E. Hamran *et al.*, "Radar Imager for Mars' Subsurface Experiment—RIMFAX," *Space Science Reviews,* vol. 216, no. 8, p. 128, 2020/11/03 2020.

[23] M. Y. Fan *et al.*, "The Mars Orbiter Subsurface Investigation Radar (MOSIR) on China's Tianwen-1 Mission," *Space Science Reviews,* Review vol. 217, no. 1, p. 17, Jan 2021.

This article has been accepted for publication in IEEE Journal of Selected Topics in Applied Earth Observations and Remote Sensing. This is the author's version which has not been fully edited and content may change prior to final publication. Citation information: DOI 10.1109/JSTARS.2024.3432535

3

> REPLACE THIS LINE WITH YOUR MANUSCRIPT ID NUMBER (DOUBLE-CLICK HERE TO EDIT) <

[24] T. Hong, Y. Su, R. Wang, S. Dai, C. Liu, and C. Li, "Overview of Mars Orbiter Subsurface Investigation Radar Data Processing Technology and Research Using Radar," *Astronomical Research & Technology,* Article vol. 18, no. 2, pp. 173-194, 2021.

[25] R. Orosei *et al.*, "Mars Advanced Radar for Subsurface and Ionospheric Sounding (MARSIS) after nine years of operation: A summary," *Planetary and Space Science,* vol. 112, pp. 98-114, 2015/07/01/ 2015.

[26] J. J. Plaut *et al.*, "Subsurface radar sounding of the south polar layered deposits of Mars," *Science,* Article vol. 316, no. 5821, pp. 92-95, Apr 2007.

[27] G. Picardi *et al.*, "Radar soundings of the subsurface of Mars," *Science,* Article vol. 310, no. 5756, pp. 1925-1928, Dec 2005.

[28] J. L. Whitten, B. A. Campbell, and G. A. Morgan, "A subsurface depocenter in the South Polar Layered Deposits of Mars," *Geophysical Research Letters,* vol. 44, no. 16, pp. 8188-8195, 2017.

[29] S. Nerozzi and J. Holt, "Buried ice and sand caps at the north pole of Mars: Revealing a record of climate change in the cavi unit with SHARAD," *Geophysical Research Letters,* vol. 46, no. 13, pp. 7278-7286, 2019.

[30] G. A. Morgan *et al.*, "Availability of subsurface water-ice resources in the northern mid-latitudes of Mars," *Nature Astronomy,* vol. 5, no. 3, pp. 230-236, 2021.

[31] T. C. Brothers and J. W. Holt, "Three-dimensional structure and origin of a 1.8 km thick ice dome within Korolev Crater, Mars," *Geophysical Research Letters,* vol. 43, no. 4, pp. 1443-1449, 2016/02/28 2016.

[32] D. E. Stillman, R. E. Grimm, and S. F. Dec, "Low-Frequency Electrical Properties of Ice−Silicate Mixtures," *The Journal of Physical Chemistry B,* vol. 114, no. 18, pp. 6065-6073, 2010/05/13 2010.

[33] A. M. Bramson *et al.*, "Widespread excess ice in Arcadia Planitia, Mars," *Geophysical Research Letters,* vol. 42, no. 16, pp. 6566-6574, 2015.

[34] Y. A. Ilyushin, R. Orosei, O. Witasse, and B. Sánchez-Cano, "CLUSIM: A Synthetic Aperture Radar Clutter Simulator for Planetary Exploration," *Radio Sci.,* Article vol. 52, no. 9, pp. 1200-1213, Sep 2017.

[35] A. Ferro, A. Pascal, and L. Bruzzone, "A Novel Technique for the Automatic Detection of Surface Clutter Returns in Radar Sounder Data," *IEEE Transactions on Geoscience and Remote Sensing,* vol. 51, no. 5, pp. 3037-3055, 2013.

[36] J. F. Nouvel, A. Herique, W. Kofman, and A. Safaeinili, "Radar signal simulation: Surface modeling with the Facet Method," *Radio Sci.,* Article vol. 39, no. 1, p. 17, Feb 2004.

[37] R. C. Aster, B. Borchers, and C. H. Thurber, *Parameter estimation and inverse problems*. Elsevier 2018.

[38] S. Shabtaie and C. Bentley, "Electrical resistivity measurements on ice stream B, Antarctica," *Annals of Glaciology,* vol. 20, pp. 129-136, 1994.

[39] M. A. Wieczorek *et al.*, "The crust of the Moon as seen by GRAIL," *Science,* vol. 339, no. 6120, pp. 671-675, 2013.

[40] S. C. Han, N. Schmerr, G. Neumann, and S. Holmes, "Global characteristics of porosity and density stratification within the lunar crust from GRAIL gravity and Lunar Orbiter Laser Altimeter topography data," *Geophysical Research Letters,* vol. 41, no. 6, pp. 1882-1889, 2014.

[41] S. J. Conway *et al.*, "Climate-driven deposition of water ice and the formation of mounds in craters in Mars' north polar region," *Icarus,* Article vol. 220, no. 1, pp. 174-193, Jul 2012.

[42] T. Matsuoka, S. Fujita, and S. Mae, "Dielectric properties of ice containing ionic impurities at microwave frequencies," *The Journal of Physical Chemistry B,* vol. 101, no. 32, pp. 6219-6222, 1997.

[43] A. Rust, J. Russell, and R. Knight, "Dielectric constant as a predictor of porosity in dry volcanic rocks," *Journal of Volcanology and Geothermal Research,* vol. 91, no. 1, pp. 79-96, 1999.

[44] M. J. Campbell and J. Ulrichs, "Electrical properties of rocks and their significance for lunar radar observations," *Journal of Geophysical Research,* vol. 74, no. 25, pp. 5867-5881, 1969.

[45] A. M. Bramson, "Radar Analysis and Theoretical Modeling of the Presence and Preservation of Ice on Mars," Ph.D., The University of Arizona, United States -- Arizona, 10931931, 2018.

Yongjiu Feng received the Ph.D. degree in Geomatics from Tongji University, Shanghai, China, in 2009.

He is currently Professor and Associate Dean of the College of Surveying and Geo-Informatics, Tongji University. His research interests include spatial modeling, synthetic aperture radar, and radar detection of the moon and deep space.
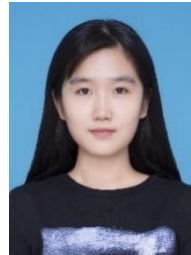
Yiyan Dong received the B.E. degree in Remote Sensing Science and Technology from Chang'an University, Xi'an, China, in 2022.

She is currently working toward the M.S. degree in Geomatics Engineering in Tongji University, Shanghai, China.

Rong Wang received the M.S. degree in Marine Sciences from Shanghai Ocean University, Shanghai, China, in 2022.

She is currently working toward the Ph.D. degree in Intelligent Science and Technology in Tongji University, Shanghai, China.

Yuze Cao received the B.E. degree in Geomatics Engineering from Wuhan University, Wuhan, China, in 2019.

He is currently working toward the M.S. degree in Civil Engineering and Water Conservancy in Tongji University, Shanghai, China.

Peiqi Wu received the M.S. degree in Geomatics Engineering from Tongji University, Shanghai, China, in 2023.

Shurui Chen received the M.S. degree in Marine Sciences from Shanghai Ocean University, Shanghai, China, in 2021.

He is currently working toward the Ph.D. degree in Surveying and Mapping Science and Technology in Tongji University, Shanghai, China.

Jingbo Sun received the B.E. degree in Geology from Tongji University, Shanghai, China, in 2023.

He is currently working toward the Ph.D. degree in Surveying and Mapping Science and Technology in Tongji University, Shanghai, China.

Yuhao Wang is currently working toward the B.E. degree in Geomatics Engineering in Tongji University, Shanghai, China.

Mengrong Xi received the B.E. degree in Geomatics Engineering from Tongji University, Shanghai, China, in 2022.

He is currently working toward the Ph.D. degree in Surveying and Mapping Science and Technology in Tongji University, Shanghai, China.

Xiaohua Tong (Senior Member, IEEE) received the Ph.D. degree from Tongji University, Shanghai, China, in 1999.

He is currently Professor at College of Surveying and Geo-Informatics, Tongji University. His research interests include photogrammetry and remote sensing, and trust in spatial data.